Medical Physics
The International Journal of Medical Physics Research and Practice

Monte Carlo simulations of the dose from imaging with GE eXplore 120 micro-CT using gate

Florian Bretin, Mohamed Ali Bahri, André Luxen, Christophe Phillips, Alain Plenevaux, and Alain Seret

Citation: Medical Physics **42**, 5711 (2015); doi: 10.1118/1.4930056
View online: http://dx.doi.org/10.1118/1.4930056
View Table of Contents: http://scitation.aip.org/content/aapm/journal/medphys/42/10?ver=pdfcov
Published by the American Association of Physicists in Medicine

---

Monte Carlo simulations of the dose from imaging with GE eXplore 120 micro-CT using GATE

Florian Bretin, Mohamed Ali Bahri, André Luxen, Christophe Phillips, Alain Plenevaux, and Alain Seret[a)]
Cyclotron Research Centre, University of Liège, Sart Tilman B30, Liège 4000, Belgium

(Received 30 October 2014; revised 31 May 2015; accepted for publication 24 August 2015; published 9 September 2015)

Purpose: Small animals are increasingly used as translational models in preclinical imaging studies involving microCT, during which the subjects can be exposed to large amounts of radiation. While the radiation levels are generally sublethal, studies have shown that low-level radiation can change physiological parameters in mice. In order to rule out any influence of radiation on the outcome of such experiments, or resulting deterministic effects in the subjects, the levels of radiation involved need to be addressed. The aim of this study was to investigate the radiation dose delivered by the GE eXplore 120 microCT non-invasively using Monte Carlo simulations in GATE and to compare results to previously obtained experimental values.
Methods: Tungsten X-ray spectra were simulated at 70, 80, and 97 kVp using an analytical tool and their half-value layers were simulated for spectra validation against experimentally measured values of the physical X-ray tube. A Monte Carlo model of the microCT system was set up and four protocols that are regularly applied to live animal scanning were implemented. The computed tomography dose index (CTDI) inside a PMMA phantom was derived and multiple field of view acquisitions were simulated using the PMMA phantom, a representative mouse and rat.
Results: Simulated half-value layers agreed with experimentally obtained results within a 7% error window. The CTDI ranged from 20 to 56 mGy and closely matched experimental values. Derived organ doses in mice reached 459 mGy in bones and up to 200 mGy in soft tissue organs using the highest energy protocol. Dose levels in rats were lower due to the increased mass of the animal compared to mice. The uncertainty of all dose simulations was below 14%.
Conclusions: Monte Carlo simulations proved a valuable tool to investigate the 3D dose distribution in animals from microCT. Small animals, especially mice (due to their small volume), receive large amounts of radiation from the GE eXplore 120 microCT, which might alter physiological parameters in a longitudinal study setup. © *2015 American Association of Physicists in Medicine.*
[http://dx.doi.org/10.1118/1.4930056]

Key words: microCT, Monte Carlo simulations, small animal dosimetry, X-ray quantification

1. INTRODUCTION

Small animal imaging techniques, such as micro computed tomography (microCT) and micro positron emission tomography (microPET), have gained significant importance in preclinical studies, as small animals are increasingly used as translational models for clinical disease and treatment research.[1] Both imaging techniques can deliver extensive amounts of radiation, especially in a longitudinal study setup. In microPET imaging of mice, the injected activity per kg can be 100 times higher than in humans in a clinical setup, resulting in far higher absorbed doses in animals.[2,3] In microCT imaging, the required resolution is typically between 50 and 100 μm, since it is used for anatomical referencing or disease staging in longitudinal studies. To achieve such a high resolution with an adequate signal-to-noise ratio, the photon flux of the X-ray tube has to be high, leading to a large radiation burden. While the absorbed dose distribution (or the S-factors for calculations of absorbed doses) of several isotopes in small animal microPET imaging has been derived in the literature[3–5] and can be applied to every microPET scan, the dose distribution resulting from microCT imaging is machine dependent and needs to be addressed for every machine. Most studies investigate the dose experimentally using thermoluminescent dosimeter (TLD) chips to derive *in vivo* point measures inside organs or in their vicinity.[6–9] Monte Carlo simulations (MCS) are a valuable tool in quantifying the 3D absorbed dose distribution in microCT non-invasively,[10,11] especially in locations or organs that are difficult to assess accurately *in vivo* due to large sensor geometries. Experimentally, bone doses can only be investigated using surface entrance doses with sensors being placed on top of the bone. With MCS, however, it is possible to obtain the spatial dose distribution within the bone. The aim of the study was to simulate the microCT eXplore 120 (GE Healthcare, Amersham, U.K./GammaMedica, Northridge, CA, USA/TriFoil Imaging, Northridge, CA, USA) using the Monte Carlo simulation software GEANT4 application for tomography emission (GATE) package. The computed tomography dose index over 100 mm (CTDI_{100}) inside a PMMA phantom was investigated, as well as the dose delivered to rats and mice, using several protocols that are regularly applied with this instrument to live animals. The results were then compared to values experimentally obtained in our lab already available in the literature.[12]

2. MATERIALS AND METHODS

All simulations of the eXplore 120 microCT were performed using GATE v6.1.[13] Since CT imaging and dose calculations involve low-energy radiation, the simulations were performed using the low-energy PENELOPE package for physics processes and interaction models[14] (for details and all cross-sections see http://geant4.web.cern.ch/geant4/G4UsersDocuments/UsersGuides/PhysicsReferenceManual/html/node64.html). The following physical processes were implemented in all performed simulations: photoelectric effect, Compton scattering, Rayleigh scattering, electron ionization, bremsstrahlung and multiple electron scattering. For details on the implemented eXplore 120 microCT the reader is referred to Bretin *et al.* or Bahri *et al.*[12,15] only information relevant to dosimetry simulations will be repeated here. The inbuilt X-ray source of the eXplore 120 microCT was a Dunlee PX1483GS (subdivision of Philips Healthcare, Amsterdam, Netherlands). Its rotating anode is made of tungsten and rhenium and has a focal spot with a diameter of 300 μm. The tube has a 5 kW peak source power and can provide tube voltages between 70 and 120 kVp (only 70, 80, and 97 kVp are available with the microCT) with a tube current range from 20 to 50 mA. Its inherent filtration is equivalent to 1.5 mm aluminum. The system's CCD detector is positioned on a rotating gantry opposite the tube at a fixed distance of 450 mm with a carbon fiber bed designed to cater for mice (25 mm width) or rats (75 mm width) in the center of rotation. The maximum axial field of view (FOV) per rotation is 55 mm (85 mm in transaxial direction). Via overlapping FOV's (15 mm on each side of the FOV) and stitching of images, the maximum axial field of view could be extended to 250 mm. The axial dose profile (collimation of the X-ray beam) was measured and its full width at half maximum (FWHM) was 74.5 mm at the center of rotation.[12] All simulations were run on a PC with a six core CPU running at 2.93 GHz, 24 GB of Ram, and Ubuntu 11.10.

2.A. Simulation geometry

The X-ray tube was reduced, for simplicity, to its focal spot and was modeled as a circular disk with a radius of 150 μm. The opening angle of the X-ray beam was determined via trigonometric calculation to be 18.80° using the measured FWHM of the axial dose profile (74.5 mm) and the distance of the tube to the center of rotation (225 mm). A detector was modeled at a distance of 450 mm to the X-ray source. Since no images had to be reconstructed from simulated data and large numbers of small detectors are computationally expensive, the detector was not subdivided and was instead modeled as a single continuous element for the purpose of verifying spectra only.

2.B. X-ray spectra

For the simulation of the X-ray spectrum at 70, 80, and 97 kVp, the spectrum simulator provided by Siemens (https://w9.siemens.com/cms/oemproducts/Home/X-rayToolbox/spektrum/Pages/radIn.aspx) based on an algorithm by Boone and Seibert[16] was used. The algorithm was developed for tungsten spectra only between 30 and 140 kV. Input parameters were 70, 80, and 97 kV peak voltages, air kerma of 0.1 Gy, and 1.5 mm equivalent Al filtration according to the filtration of the microCT.

2.C. Half-value layer (HVL)

In order to validate the spectra, the HVL was determined via simulation and physical measurements. The HVL represents the thickness of a material reducing the intensity of radiation by absorption and scattering by one half. In radiology, it is usually measured using aluminum (Al) for beam quality control purposes.

2.C.1. Simulation

For the determination of the HVL using simulations, a 60×60 mm box of Al was inserted into the beam path at 60 mm distance to the X-ray source with varying thicknesses (3.8/4.2/4.6 mm Al at 70 kVp, 4.6/5/5.4 mm Al at 80 kVp, and 5.8/6.2/6.6 mm Al at 97 kVp). The three thicknesses were selected on the basis of the results of the physical measurements. An ideal single lead detector at a distance of 225 mm with a size of $80 \times 80 \times 1$ mm was used for stopping and counting photons, and a total amount of 6×10^{07} photons were simulated per simulation. The simulation was repeated three times for each Al thickness and the HVL of each spectrum was determined via linear regression. The mean HVL and standard deviation were reported.

2.C.2. Physical measurement

The HVL of the PX1483GS X-ray tube at 70, 80, and 97 kVp was physically measured with the X-ray quality control device Black Piranha from RTI Electronics (RTI AB, Mölndal, Sweden). The HVL measurement is based on the attenuation difference in several filters. The sensor was placed at the center of rotation of the gantry on the carbon fiber bed with the X-ray tube in stationary top position above the sensor. The tube was triggered with a tube current of 50 mA and an exposure time of 100 ms at the respective tube voltage with five measurements per tube voltage setting.

2.D. Phantoms

CT images of three phantoms in Analyze 7.5 format were used for dose simulations: a custom built PMMA phantom, a representative mouse, and a representative rat.

Table I. Protocol settings.

Protocol	Voltage (kV)	Current (mA)	Exposure time (ms)	Projections (views)	Gantry rotation (°)	Voxel size (μm)
Fast scan 220 (P1)	70	32	16	220	192	100
Fast scan 360 (P2)	70	32	16	360	360	100
Soft tissue fast scan (P3)	70	50	32	220	192	50
Soft tissue step and shoot (P4)	80	32	16	220	192	100

The cylindrical PMMA phantom had a diameter of 50 mm, a length of 200 mm, nine continuous axial boreholes for physical sensor placement and was designed to mimic the size of an average rat. The PMMA phantom has previously been used for physical dose measurements in microCT and was described in detail in Bretin *et al.*[12] All images were acquired using the eXplore 120 microCT. The images were implemented into the rotational center between source and detector and were rotated instead of the source-detector geometry according to the settings (Table I) of the four simulated acquisition protocols (P1–P4), which were also experimentally investigated in Bretin *et al.*[12]

The images included the microCT bed as the attenuation inside the bed decreases the amount of X-ray quanta reaching the subject on the table. In Fig. 1, all three images, which were down-sampled for computational speed, are displayed: the PMMA phantom ($0.7019\times0.7019\times3.1999$ mm voxel size), a representative mouse ($0.3996\times0.3996\times0.3996$ mm voxel size), and a representative rat ($0.7992\times0.7992\times0.7992$ mm voxel size). Images in numerical values (not converted to Hounsfield units) were segmented using a threshold based approach and the ranges of pixel values (PV) of segmented structures were related to either existing materials or newly implemented materials in the GATE material database. Since the soft tissue contrast between organs (with the exception of lung) in mouse and rat was low as can be seen in Fig. 2, organs were manually segmented by placing spheres in the center of organs. The PV ranges inside the spheres in the respective organs were derived.

2.E. Dose simulations

The four different protocols (P1–P4) were implemented and simulated using all three above mentioned phantoms (PMMA, mouse, rat). In the starting position (0° rotation) of each simulation, the X-ray source was located in the top position above the various phantoms. The phantoms were then rotated anticlockwise during the simulation according to protocol settings. A total amount of 6×10^{07} photons was simulated in each simulation, which was considered to be a trade-off between long computation times and noise levels. The output of simulations was a co-registered Analyze7.5 image of the spatial dose distribution with the same size and resolution as the original input CT image. Single field of view (sFOV) acquisitions and multiple fields of view (mFOV) acquisitions were simulated. The mFOV simulations consisted of several independently performed sFOV simulations with the source translated in the axial direction according to the machine settings of the eXplore 120 microCT. The overlap between images (15 mm on each side) used for stitching images together was therefore taken into account. The dose maps of all sFOV building the mFOV acquisition were then added up numerically to form one dose map. For the PMMA phantom, one sFOV simulation was performed with each protocol, along with one mFOV consisting of five sFOV simulations using P1. The mFOV of the PMMA phantom using other protocols was not investigated because of long computation times. Due to memory leak issues, the resolution of the image of the PMMA phantom had to be

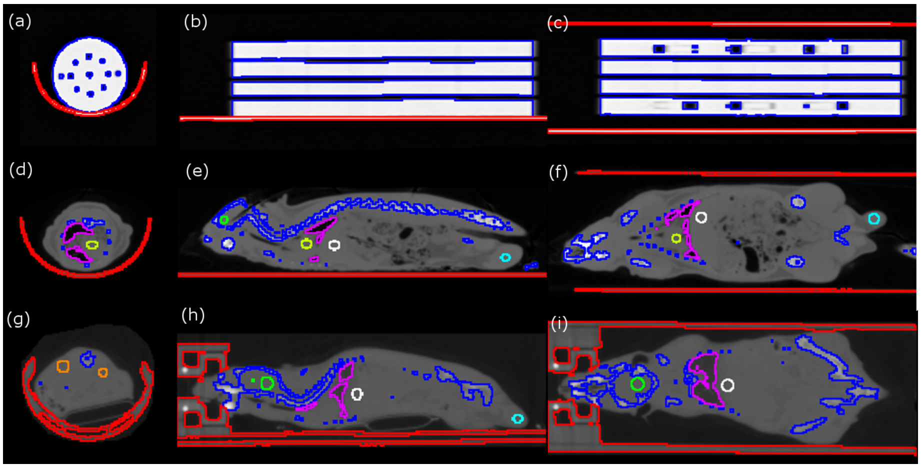

Fig. 1. Down-sampled, segmented CT input images of phantom: (a) transversal, (b) sagittal, and (c) coronal plane; rat: (d) transversal, (e) sagittal, and (f) coronal plane; and mouse: (g) transversal, (h) sagittal, and (i) coronal plane. Note that the pixel size of the three sets of images is different (see text).

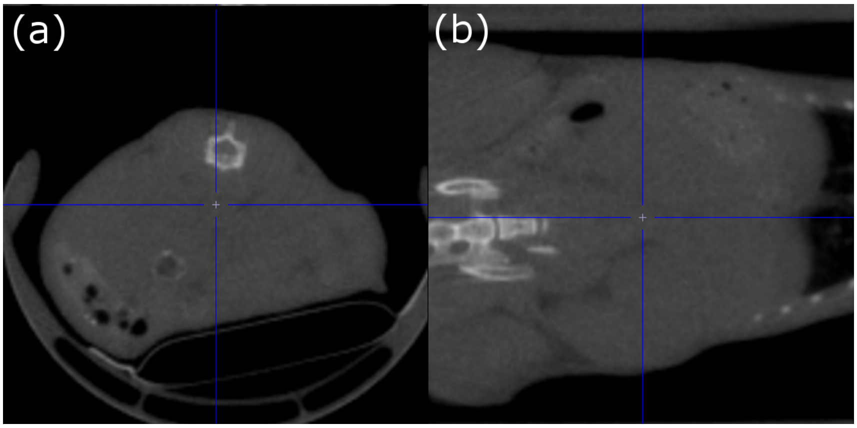

FIG. 2. Low soft tissue contrast in (a) transversal and (b) coronal plane of mouse phantom.

decreased to a voxel size of 1.4218×1.4218×3.1999 mm for simulations using P2. For rodent simulations, mFOV scans were performed with three sFOV for mice and five sFOV for rats using all protocols (P1–P4). The relative uncertainty in mFOV images was calculated according to Chetty *et al.*[17] as commonly conducted in GATE. All simulated doses and their corresponding uncertainty were read out from the dose maps and uncertainty maps using the same volumes-of-interest (VOIs) that were used for the segmentation of the respective phantom (Sec. 2.D, Fig. 1). Standard deviations of organ doses represent the standard deviation of the dose inside the respective VOI. All presented values are in mean ± standard deviation.

2.F. Scaling of dose maps and computed tomography dose index (CTDI)/multiple scan average dose (MSAD) calculation

Since only a fraction of the real amount of photons emitted by the X-ray source was simulated to decrease simulation time, the resulting dose maps were scaled using measured data. Eight simulated axial dose profiles $D(i)$ along the scanner axis z were extracted from the unscaled dose map of the PMMA phantom around the center hole inside the phantom, which were averaged and then used to compute the CTDI analogue to[12]

$$\mathrm{CTDI}_{100} = \frac{1}{N\cdot T}\sum_{i=-50}^{50} D(i).$$

$N\cdot T$ is usually defined as the nominal beam width, but in this case was set equal to the width of the acquired FOV of 55 mm as in Ref. 12. For each acquisition protocol Pi ($i=1,\ldots,4$), the dose map was then scaled by the ratio between the computed $\mathrm{CTDI}_{\mathrm{sim},I}$ based on simulated data and the physically measured $\mathrm{CTDI}_{\mathrm{exp},i}$ available in Ref. 12 in the same center position, similar to Taschereau *et al.*[10] The obtained scaling factors $f_{s,i}$ were applied to all simulations of the respective protocol,

$$f_{s,i} = \frac{\mathrm{CTDI}_{\mathrm{exp},i}}{\mathrm{CDTI}_{\mathrm{sim},i}}.$$

For all sFOV simulations of the PMMA phantom, the CTDI was computed in nine transaxial positions, as described above. Additionally, the FWHM of all extracted dose profiles was determined. The MSAD of P1 was calculated using the dose profile $D_N(t)$ of the mFOV acquisition N as follows:

$$\mathrm{MSAD} = \frac{1}{I}\sum_{t=-\frac{I}{2}}^{+\frac{I}{2}} D_N(t),$$

where I equals the width of the central sFOV of 55 mm.

Standard deviations of the extracted dose profiles and the CTDI_{100} were calculated based on the eight derived dose profiles around the respective transaxial position; the standard deviation of the transaxial CTDI_{100} was based on the CTDI_{100} of all nine transaxial positions.

3. RESULTS

3.A. Simulated X-ray spectra

Figure 3 displays the X-ray spectra at 70, 80, and 97 kVp tube voltage simulated using the Siemens X-ray tool. Characteristic tungsten emission peaks can be observed for 80 and 97 kVp.

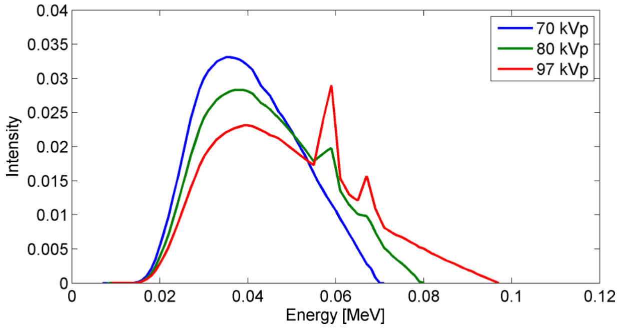

FIG. 3. Simulated X-ray spectra at 70, 80, and 97 kVp.

TABLE II. Physically measured tube parameters and HVL (MHVL) and simulated HVL (SHVL).

Tube voltage (kVp)	70	80	97
Measured tube voltage (kVp)	70.60 ± 0.06	79.92 ± 0.07	96.99 ± 0.08
Measured exposure (ms)	93.93 ± 1.50	94.64 ± 0.42	94.84 ± 0.55
Measured dose (mGy)	0.51 ± 0.01	0.73 ± 0.00	1.22 ± 0.01
MHVL (mm Al)	4.22 ± 0.02	4.88 ± 0.01	5.80 ± 0.01
SHVL (mm Al)	4.29 ± 0.00	5.06 ± 0.00	6.03 ± 0.00
Difference MHVL to SHVL (%)	1.6	3.7	3.9

3.B. Half-value layer

The half-value layers of the spectra of the X-ray tube PX1483GS were measured and derived via simulations. Both results are displayed in Table II.

The simulation of the HVL showed a highly linear relationship between the percentage of all emitted photons detected and the thickness of the aluminum box inside the beam path with $R^2 > 0.999$ for all tube voltages (as can be seen in Fig. 4). The resulting standard deviation of the simulated HVL stayed below 1×10^{-04}. The differences between measured values and simulated values amounted to 1.6% for 70 kVp, 3.7% for 80 kVp, and 3.9% for 97 kVp. The computation times of a HVL simulation for a single layer thickness was approximately 3 h.

3.C. Dose simulation

In Table III, the PV of materials inside the phantoms obtained by segmentation of the Analyze7.5 input images is displayed, along with the assigned materials of the GATE material database. PV of all organs (with the exception of lung) overlapped and were summarized as soft tissue. Bone structures could not be resolved due to the limited resolution of the images and the whole skeleton was summarized as bone. A material definition from the MOBY phantom[18] of lung tissue was assigned to the lung pixel value range of mouse and rat. All other material compositions were taken from the GATE material database.

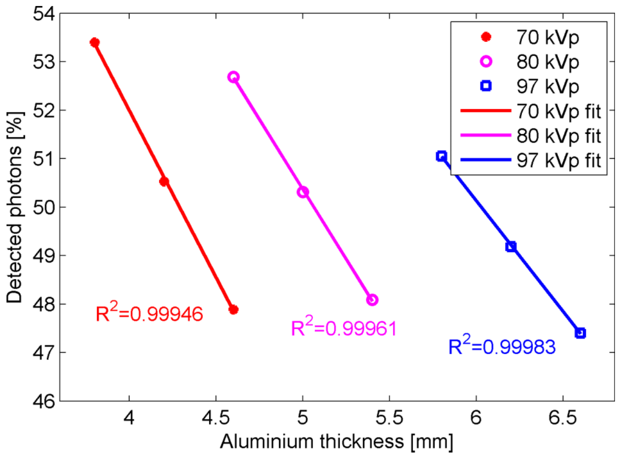

FIG. 4. Simulation of HVL for 70, 80, and 97 kVp including fit and coefficient of determination (R^2).

In Table IV the scaling factors, f_s (the ratio between the experimentally derived CTDI_{100} and the CTDI_{100} obtained from unscaled simulated dose maps), and the scaled and averaged CTDI_{100} of the center position including the transaxial average for P1–P4 are displayed. The averaged MSAD including the transaxial average was simulated for P1 only. The highest radiation was delivered by P3, followed by P2. Standard deviation for 192° gantry rotation in the transaxial average CTDI_{100} was found to be increased compared to the 360° rotation protocols.

In Fig. 5, simulated dose profiles inside the PMMA phantom of P1 are displayed. The CTDI_{100} was determined to be 20.25 ± 0.44 mGy and the MSAD (5 sFOV acquisition) was 28.75 ± 1.32 mGy. Peak dose point value in the mFOV acquisition was 37.9 mGy. Dose profiles in positions on the left side of the phantom (side of gantry rotation) showed higher maximum dose values due to the limited 192° anticlockwise rotation of the gantry for sFOV and mFOV acquisitions.

In Figs. 6(a) and 6(b), a comparison of sFOV (P1 and P3) and mFOV (P1) dose profiles of the center position inside the PMMA phantom taken from Bretin *et al.*[12] (physically measured) and derived by simulations is presented. In Fig. 6(c), the CTDI_{100} of all protocols obtained from physical measurements[12] and by simulations is displayed for the center position and the transaxial average. All derived values agreed within an error range of 2%.

Figure 7 displays organ doses including the whole body dose simulated in the mouse and the rat phantom using P1 to P4. Similar to the phantom results, P3 delivered the highest amount of radiation in both species. The largest dose was received by the bones, with an average of 459.13 ± 96.37 mGy from P3 in mice due to the high density of bone (298.69 ± 91.87 mGy in rats from P3). The average whole body dose delivered by P3 in mice was 188.70 ± 112.05 mGy (118.89 ± 71.01 mGy in rats). The average soft tissue organ dose was 159.42 ± 43.91 mGy in mice from P3 (128.01 ± 36.67 mGy in rats) with the testes receiving the lowest dose and the lung receiving the largest dose. The same pattern was found for all protocols and both species, with P1 delivering a smaller dose by a factor of 2.8, P2 by a factor of 1.3, and P4 by a factor of 2.1.

Depending on the protocol and phantom used, the computation time for a single field of view varied between 24 and 96 h (P1 24 h and P3 96 h). The average uncertainty inside the phantoms in all dose simulations stayed below 14% (PMMA-phantom < 4.2%, rat < 5.4%, mouse < 13.2% for

TABLE III. Pixel values of materials in phantoms.

	Air	Lung tissue	PMMA	Carbon fiber	Soft tissue	Bone
PMMA phantom (NR)	−32 768 to 624	—	624 to 20 295	20 295 to 32 768	—	—
Rat (NR)	−15 750 to −13 607	−13 607 to −5 835	—	−5 835 to −1 712	−1712 to 2107	2 107 to 32 767
Mouse (NR)	−17 579 to −9 380	−9 380 to −3 888	−3 888 to −1 000	—	−1000 to 1500	1 500 to 32 767
Material database	Air	Lung MOBY	PMMA	Carbon fiber	Soft tissue	Spine bone

P1; other protocols showed lower uncertainty due to greater photon flux).

4. DISCUSSION

In this study, we investigated the radiation dose delivered by the eXplore 120 microCT using Monte Carlo simulations. X-ray spectra for a tungsten anode were simulated with a publicly available tool provided by Siemens, based on an algorithm by Boone and Seibert[16] and validated with physical measurements and simulations of the HVL. Although the anode of the X-ray tube PX1483GS contains tungsten and rhenium and the simulated X-ray spectra at 70, 80, and 97 kVp tube voltage were based on data for tungsten anodes only, the measured HVL and simulated data agreed closely. Differences in HVL of 1.6% at 70 kVp, 3.7% at 80 kVp, and 3.9% at 97 kVp could be observed, which is in the range of the inaccuracy of ±10% or ±0.2 mm Al provided by the manufacturer of the sensor for 70 and 80 kVp. Nonetheless, the error between experimental data and simulated data increased with tube voltage. The simulated X-ray spectra are for tungsten anodes only, and the material characteristic peaks in an X-ray spectrum become more apparent at higher tube voltages, as can be seen in Fig. 3. The peaks characteristic for rhenium are slightly different than for tungsten, thereby explaining the larger difference observed at higher tube voltages.

Deriving pixel value ranges of structures or organs inside the low-contrast microCT images by segmentation proved challenging. Many structures contained similar pixel values and overlapped. All segmented organs, with the exception of lung, had to be summarized as soft tissue inside the image. All bone structures including the bone marrow were assigned the same material composition due to overlapping pixel values and the low resolution of the down-sampled phantoms. The material composition of spine bone (implemented in the GATE material database) was assigned to the whole skeleton since its density of 1.42 g/cm^3 represented an approximate average of all bone densities implemented in GATE. Analytical phantoms instead of voxelized phantoms, such as the MOBY and ROBY phantom,[19] would have enabled us to differentiate between more structures, but these are commercial products nowadays and were not available to us.

The derived CTDI$_{100}$ values inside the PMMA phantom (see Table IV) confirmed the physically measured values available in Ref. 12. Although the center CTDI$_{100}$ could not differ from the measured value due to scaling of the dose maps to that particular value, the transaxial averages of 192° and 360° rotation protocols also agreed [see Fig. 6(c)], proving that the simulated dose deposition inside the phantom reflects the measured situation. Standard deviations were slightly higher in simulated transaxial averages compared to physically measured transaxial averages, which could be related to noise originating from the approach of simulating only a fraction of the total amount of photons emitted and scaling afterwards. Simulations with the real photon flux of the X-ray tube could potentially result in improved results due to a higher signal-to-noise ratio; however, very long computation times are to be expected. The simulated mFOV dose profile of protocol P1 in the center position of the PMMA phantom matched the measured dose profile from Ref. 12 closely. The measured dose profile was derived by measuring a sFOV dose profile using MOSFET sensors inside the PMMA phantom, which was then used to theoretically construct the mFOV dose profile by superposition and shifting of the sFOV dose profile. The agreement between both mFOV dose profiles confirmed the assumptions made regarding the additive nature of the dose profiles inside the homogenous medium, and renders phantom measurements and simulations of mFOV acquisitions in phantoms redundant since the mFOV dose profile can be obtained by simple superposition of sFOV dose profiles. The calculated MSAD (based on simulations in the center FOV) consequently matched the experimental value within an error range of 5%. It is to be expected that simulated mFOV acquisitions would produce similarly accurate results for all other protocols due to the very close agreement of sFOV dose profiles across all protocols. The

TABLE IV. Scaling factor, CTDI$_{100}$, and MSAD derived by simulations using the PMMA phantom.

	P1	P2	P3	P4
Scaling factor f_s	9816.1	12 642.0	13 547.8	14 228.1
CTDI center (mGy)	20.25 ± 0.44	30.09 ± 0.29	55.81 ± 0.48	28.56 ± 7.41
CTDI transaxial (mGy)	20.12 ± 2.59	30.94 ± 0.19	55.58 ± 7.82	28.13 ± 3.71
MSAD center (mGy)	28.75 ± 1.32	—	—	—
MSAD transaxial (mGy)	28.76 ± 4.05	—	—	—

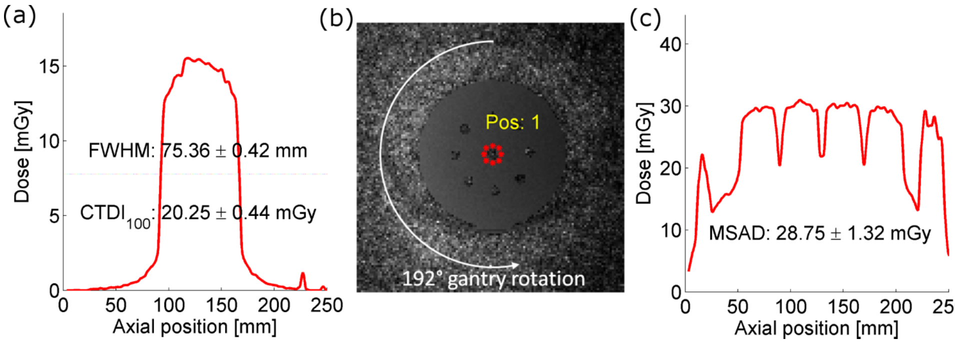

FIG. 5. Simulated average dose profiles of P1 in PMMA phantom with (a) center position sFOV, (b) simulated dose map including positions for data extraction for center CTDI calculation, and (c) simulated mFOV.

mFOV acquisitions of protocols P2 to P4 were therefore not simulated to save computation time. However, the simulated mFOV dose profile of protocol P1 showed dose deposition peaks on either side of the profile outside of the phantom boundaries in air. They originated from the first and last sFOV acquisition in the axial scanner direction (translation of the source in axial direction of ±8 cm), where the beam was directed at the boundary between air and PMMA. Even when the source was located in the center, the dose was deposited in the air beyond the phantom boundaries. The artifacts could be related to edge effects on material boundaries and scatter from inside the phantom. There was no impact from the artifacts on the calculation of the MSAD, since the MSAD was calculated in the central portion (central sFOV) of the dose profile. The derived CTDI$_{100}$ and MSAD values using the custom build PMMA phantom cannot be compared to values obtained with clinical CT systems, since the geometry of the phantom used is much smaller and the tube currents used in microCT are higher. Therefore, the CTDI$_{100}$ and MSAD presented here are much higher compared to clinical values derived using the standard CTDI phantoms and clinical CT systems.

The derived scaling factors (f_s, see Table IV) were different for the three protocols using 70 kVp (P1–P3), which can be explained by the different tube current and exposure settings of, for example, P1 and P3. The scaling factors were derived from dose information only and not from dose normalized per mAs, which would have resulted in more similar values. The difference between P1 and P2 (same mAs setting) can be explained by the different CTDI$_{100}$ normalized per mAs found in the physically measured data[12] (0.1798 mGy/mAs for P1 and 0.1676 mGy/mAs for P2), which also impacted the scaling factor for the simulation.

The derived doses from the animal phantoms of mouse and rat showed that significant doses are inflicted on both species in a typical microCT acquisition. Smaller animals in particular (such as mice) receive a large amount of radiation due to their small volume, with bone doses of up to 459.13 ± 96.37 mGy (P3). The whole body received a total amount of radiation of 68.39 ± 40.89 mGy (mouse, P1) and 43.07 ± 25.79 mGy (rat, P1), which is far more than predicted by the MSAD for P1 (3 sFOV for mouse: 28.49 ± 1.36 mGy; 5 sFOV for rat: 28.75 ± 1.32 mGy). This is related to the difference in volume between the PMMA phantom, the mouse, and the rat. The PMMA phantom has a total volume of 392.69 cm^3, the rat 258.18 cm^3, and the mouse 18.76 cm^3. Boone *et al.*[20] performed Monte Carlo simulations with a homogenous small animal model of different diameters (5–40 mm) and also found that the dose increases with a decreasing animal diameter. Derived rat organ doses are therefore closer to the MSAD due to the more similar volume. The average soft tissue organ dose in mice was 159.42 ± 43.91 and 128.02 ± 36.67 mGy in rats using P3. High energy protocols such as P3 (with longer exposure and a larger tube current compared to P1) result in higher radiation burdens. The large standard deviations in all derived organ doses might simply be a result of the 192° gantry rotation, which results in higher doses on one side of the animal. Another factor might be the approach

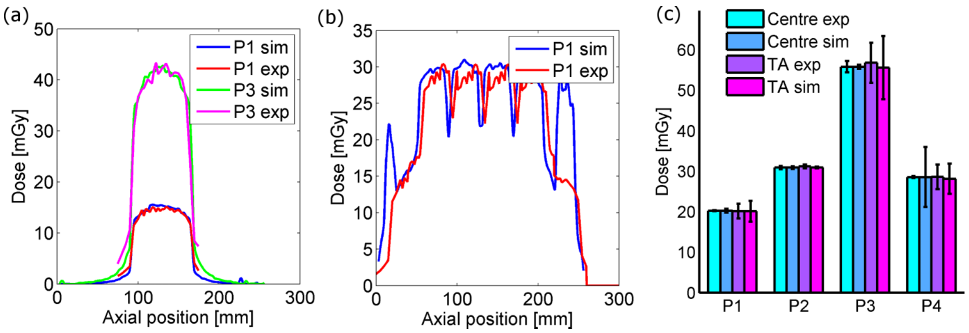

FIG. 6. Experimental (exp) and simulated (sim) data of (a) center position inside PMMA phantom for sFOV of P1 and P3, (b) mFOV using P1, and (c) CTDI of all protocols for center position and the transaxial average (TA).

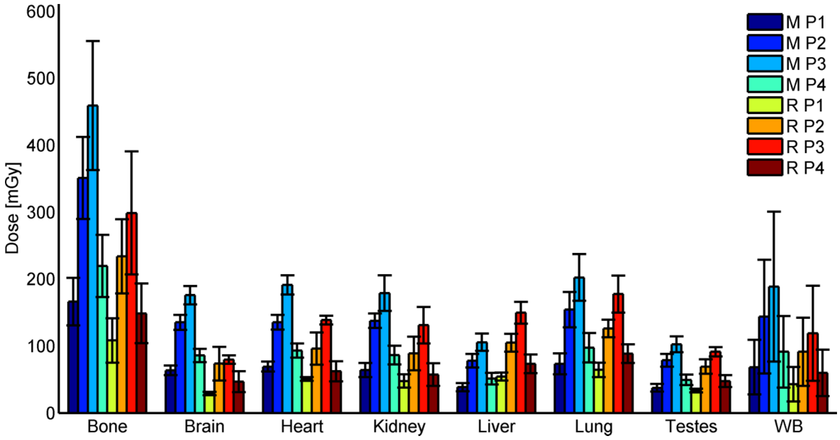

FIG. 7. Organ doses derived from mFOV acquisitions with P1 to P4 in mice (3 sFOV) and with P1 and P3 in rats (5 sFOV), WB = whole body, M = mouse, R = rat.

of simulating only a fraction of the photons and scaling afterwards, which results in a lower signal-to-noise ratio than if the real number of photons had been simulated. Analytical animal models, where different material compositions can be easily assigned to different organs, might improve the accuracy of the results and they should be implemented for future studies. Additionally, partial volume effects could have influenced especially the derived doses for bone, since the structures are small and were fully segmented using thresholding. The sphere segmentation in the center of organs applied to soft tissue organs counteracts partial volume effects, since the effect is largest on boundaries between structures. Using a high resolution image as a phantom will be part of future studies to minimize partial volume effects.

When comparing the mouse doses derived by this study for the 360° rotation protocol P2 to data from a 70 kVp protocol (2 mm Al filtration, 360 × 0.5 s exposures, and 0.5 mA) derived by Taschereau *et al.*[10] for another microCT, absolute total body doses delivered by the eXplore 120 microCT are slightly larger, but the dose per mAs is lower (total body dose of 0.78 mGy/mAs vs 1.03 mGy/mAs from Taschereau *et al.*). The protocols are different; the eXplore 120 microCT uses a much higher current while the exposure per projection is much shorter compared to the machine simulated by Taschereau *et al.* The higher absolute doses might also be a result of the soft beam of the eXplore, as it has 0.5 mm Al less filtration.

The lethal level of radiation for mice is considered to be a single total body entrance dose of 6 Gy.[21] While such an excessive amount is not exceeded using microCT, studies have shown that lower amounts of radiation can lead to, for example, DNA damage in cells with about 40 DNA double-strand breaks per 1 Gy/cell.[22] Foster and Ford[23] showed in their study that a longitudinal imaging session consisting of four consecutive scans every four days with a maximum of 300 mGy delivered per scan did not significantly impact tumor growth. However, tumor growth could be an insufficiently sensitive parameter as biological effects might be still present before tumor growth is effected.[6] Chen *et al.* found a change in protein expressions of mouse thymocytes after a whole body irradiation with 75 mGy X-rays,[24] which are in the dose range of the protocols investigated here. Wan *et al.*[25] investigated the effects of low-dose radiation on signal transduction of neurons in mouse hypothalamus using 75 mGy X-rays and found that the low-dose radiation may potentiate the activity of the neurons in mouse hypothalamus. When microCT is combined with microPET imaging in a longitudinal study, far higher total body doses can be reached, depending on the number of scans and the injected activity in microPET scans.[26] More research needs to be conducted in low-level radiation biology to fully understand the biological consequences induced by radiation delivered from microCT and microPET imaging, especially when combined in longitudinal studies due to the increased delivered dose.

In future studies, an analytical small animal model should be used to allow different material compositions to be assigned to all organs and to derive more organ doses, especially to the radiosensitive bone marrow. Simulations with the appropriate photon flux of the respective X-ray tube might increase the signal-to-noise ratio in dose maps and produce more accurate results.

In conclusion, we established a valid Monte Carlo simulation model of the eXplore 120 microCT for tube voltages of 70, 80, and possibly 97 kVp (no dose calculations were simulated using 97 kVp). Simulated dose profiles and consequently the CTDI_{100} and MSAD in a PMMA phantom agreed closely with published physically derived results. Monte Carlo simulations proved a valuable tool to noninvasively derive organ doses in rats and mice. Researchers using the eXplore 120 microCT can expect significant radiation doses in mice from a single acquisition, with total body doses of 189 mGy using P3. In particular, bones in mice are exposed to high radiation burdens of up to 459 mGy. The additional radiation from microCT in longitudinal dual modality studies should always be taken into account in order to avoid overexposures of animals that might compromise the outcome of the study.

ACKNOWLEDGMENTS

Florian Bretin is supported by Marie Curie Initial Training Network (MCITN) “Methods in Neuroimaging” under Grant No. #MC-ITN-238593. Alain Plenevaux is a research director from FRS-FNRS Belgium. Special thanks to Francoise Malchair (Zephyra, Liège, Belgium) for providing us with the Black Piranha device and conducting the measurement with us. We would like to thank all reviewers for their valuable input. None of the authors have any conflict of interest.

[a] Author to whom correspondence should be addressed. Electronic mail: aseret@ulg.ac.be; Telephone: + 32-4-3663705.

[1] W. Koba, L. A. Jelicks, and E. J. Fine, "MicroPET/SPECT/CT imaging of small animal models of disease," Am. J. Pathol. **182**, 319–324 (2013).

[2] P. Zanotti-Fregonara, A. A. Lammertsma, and R. B. Innis, "Suggested pathway to assess radiation safety of 18F-labeled PET tracers for first-in-human studies," Eur. J. Nucl. Med. Mol. Imaging **40**, 1781–1783 (2013).

[3] R. Taschereau and A. F. Chatziioannou, "Monte Carlo simulations of absorbed dose in a mouse phantom from 18-fluorine compounds," Med. Phys. **34**, 1026 (2007).

[4] M. G. Stabin, T. E. Peterson, G. E. Holburn, and M. A. Emmons, "Voxel-based mouse and rat models for internal dose calculations," J. Nucl. Med. **47**, 655–659 (2006).

[5] E. Larsson, S. Strand, M. Ljungberg, and B. Jönsson, "Mouse S-factors based on Monte Carlo simulations in the anatomical realistic MOBY phantom for internal dosimetry," Cancer Biother. Radiopharm. **22**, 438–442 (2007).

[6] V. Kersemans, J. Thompson, B. Cornelissen, M. Woodcock, P. D. Allen, N. Buls, R. J. Muschel, M. A. Hill, and S. C. Smart, "Micro-CT for anatomic referencing in PET and SPECT: Radiation dose, biologic damage, and image quality," J. Nucl. Med. **52**, 1827–1833 (2011).

[7] S. D. Figueroa, C. T. Winkelmann, W. H. Miller, W. A. Volkert, and T. J. Hoffmann, "TLD assessment of mouse dosimetry during microCT imaging," Med. Phys. **35**, 3866–3874 (2008).

[8] S. K. Carlson, K. L. Classic, C. E. Bender, and S. J. Russell, "Small animal absorbed radiation dose from serial micro-computed tomography imaging," Mol. Imaging Biol. **9**, 78–82 (2007).

[9] I. Willekens, N. Buls, T. Lahoutte, L. Baeyens, C. Vanhove, V. Cavaliers, R. Deklerck, A. Bossuyt, and J. de Mey, "Evaluation of the radiation dose in microCT with optimization of the scan protocol," Contrast Media Mol. Imaging **5**, 201–207 (2010).

[10] R. Taschereau, P. L. Chow, and A. F. Chaziioannou, "Monte Carlo simulations of dose from microCT imaging procedures in a realistic mouse phantom," Med. Phys. **33**, 216–224 (2006).

[11] M. Hupfer, D. Kolditz, T. Nowak, F. Eisa, R. Brauweiler, and W. Kalender, "Dosimetry concepts for scanner quality assurance and tissue dose assessment in micro-CT," Med. Phys. **39**, 658–670 (2012).

[12] F. Bretin, G. Warnock, A. Luxen, A. Plenevaux, A. Seret, and M. A. Bahri, "Performance evaluation and x-ray dose quantification for various scanning protocols of the GE eXplore 120 micro-CT," IEEE Trans. Nucl. Sci. **60**, 3235–3241 (2013).

[13] S. Jan, D. Benoit, E. Becheva, T. Carlier, F. Cassol, P. Descourt, T. Frisson, L. Grevillot, L. Guigues, L. Maigne, C. Morel, Y. Perrot, N. Rehfeld, D. Sarrut, D. R. Schaart, S. Stute, U. Pietrzyk, D. Visvikis, N. Zahra, and I. Buvat, "GATE V6: A major enhancement of the GATE simulation platform enabling modelling of CT and radiotherapy," Phys. Med. Biol. **56**, 881–901 (2011).

[14] J. Baró, J. Sempau, J. M. Fernandez-Varea, and F. Salvat, "PENELOPE: An algorithm for Monte Carlo simulation of the penetration and energy loss of electrons and positrons in matter," Nucl. Instrum. Methods Phys. Res., Sect. B **100**, 31–46 (1995).

[15] M. A. Bahri, G. Warnock, A. Plenevaux, P. Choquet, A. Constantinesco, E. Salmon, A. Luxen, and A. Seret, "Performance evaluation of the General Electric eXplore CT 120 micro-CT using the vmCT phantom," Nucl. Instrum. Methods Phys. Res., Sect. A **648**, S181–S185 (2011).

[16] J. M. Boone and J. A. Seibert, "An accurate method for computer-generating tungsten anode x-ray spectra from 30 to 140 kV," Med. Phys. **24**, 1661–1670 (1997).

[17] I. J. Chetty, M. Rosu, M. L. Kessler, B. A. Fraass, R. K. Ten Haken, F. M. Kong, and D. L. Mc Shan, "Reporting and analyzing statistical uncertainties in Monte Carlo-based treatment planning," Int. J. Radiol. Oncol., Biol., Phys. **65**, 1249–1259 (2006).

[18] W. P. Segars, B. M. W. Tsui, E. C. Frey, and G. Allan Johnson, "Development of a 4-D digital mouse phantom for molecular imaging research," Mol. Imaging Biol. **6**, 149–159 (2004).

[19] M. A. Keenan, M. G. Stabin, W. P. Segars, and M. J. Fernald, "RADAR realistic animal model series for dose assessment," J. Nucl. Med. **51**, 471–476 (2010).

[20] J. M. Boone, O. Velazques, and S. R. Cherry, "Small-animal x-ray dose from micro-CT," Mol. Imaging **3**, 149–158 (2004).

[21] E. L. Ritman, "Micro-computed tomography-current status and developments," Annu. Rev. Biomed. Eng. **6**, 185–208 (2004).

[22] K. M. Prise, G. Schettino, M. Folkard, and K. D. Held, "New insights on cell death from radiation exposure," Lancet Oncol. **6**, 520–528 (2005).

[23] W. K. Foster and N. L. Ford, "Investigating the effect of longitudinal micro-CT imaging on tumor growth in mice," Phys. Med. Biol. **56**, 315–326 (2011).

[24] S. L. Chen, L. Cai, Q. Y. Meng, S. Xu, H. Wan, and S. Z. Liu, "Low-dose whole-body irradiation (LD-WBI) changes protein expression of mouse thymocytes: Effect of a LD-WBI-enhanced protein RIP10 on cell proliferation and spontaneous or radiation-induced thymocyte apoptosis," Toxicol. Sci. **55**, 97–106 (2000).

[25] H. Wan, S. L. Gong, and S. Z. Liu, "Effects of low dose radiation on signal transduction of neurons in mouse hypothalamus," Biomed. Environ. Sci. **14**, 248–255 (2001).

[26] F. Bretin, T. Mauxion, G. Warnock, M. A. Bahri, L. Libert, C. Lemaire, A. Luxen, M. Bardiès, A. Seret, and A. Plenevaux, "Hybrid microPET imaging for dosimetric applications in mice: Improvement of activity quantification in dynamic microPET imaging for accelerated dosimetry applied to 6-[18F]Fluoro-L-DOPA and 2-[18F]Fluoro-L-Tyrosine," Mol. Imaging Biol. **16**, 383–394 (2014).